

Article

Study on the Bending Performance of High-Strength and High-Ductility CRE-Reinforced Concrete Beams

Xiao Zhang ^{1,2}, Youkun Sun ^{3,*} , Xiaoxia Yang ³, Lele Sun ^{3,*} and Peijun Wang ³¹ School of Qilu Transportation, Shandong University, Jinan 256001, China² State Key Laboratory for Geomechanics and Deep Underground Engineering, China University of Mining and Technology (Beijing), Beijing 100083, China³ School of Civil Engineering, Shandong University, Jinan 256001, China; pjwang@sdu.edu.cn (P.W.)

* Correspondence: sunyoukun@mail.sdu.edu.cn (Y.S.); lelesun117@163.com (L.S.)

Abstract: Constant resistance energy (CRE) steel reinforcement has a yield strength of up to 750 MPa and an ultimate elongation of more than 20%. CRE reinforcement overcomes the contradiction between high yield strength and high uniform elongation of ordinary high-strength bars. This paper explores the flexural performance and load-carrying mechanisms of CRE-reinforced concrete beams through a series of experiments, while also presenting a theoretical analytical method for such specimens. Flexural tests on six CRE-reinforced concrete beams and two control tests on hot-rolled ribbed bar 400 (HRB400)-reinforced concrete beams were conducted in this paper. The study examines the influence of the shear–span ratio and reinforcement type on the mechanical response of the beams, including cracking load, yield load, and ultimate load, while analyzing the variation patterns of concrete strain and reinforcement strain. The experimental results demonstrate that as the shear–span ratio decreases, the crack resistance and load-carrying capacity of CRE-reinforced concrete beams improve. Under equivalent conditions, CRE-reinforced concrete beams exhibit higher load-carrying capacity compared to HRB-reinforced concrete beams, surpassing the latter by approximately 43% in terms of ultimate load. Additionally, this paper proposes a calculation method for the mechanical response of NPR-reinforced concrete beams and compares the theoretical values with the experimental values. The differences between the two are within 13%, which proves the reliability of the calculation method.



Citation: Zhang, X.; Sun, Y.; Yang, X.; Sun, L.; Wang, P. Study on the Bending Performance of High-Strength and High-Ductility CRE-Reinforced Concrete Beams. *Buildings* **2023**, *13*, 2746. <https://doi.org/10.3390/buildings13112746>

Academic Editor: Yann Malecot

Received: 19 September 2023

Revised: 13 October 2023

Accepted: 19 October 2023

Published: 30 October 2023



Copyright: © 2023 by the authors. Licensee MDPI, Basel, Switzerland. This article is an open access article distributed under the terms and conditions of the Creative Commons Attribution (CC BY) license (<https://creativecommons.org/licenses/by/4.0/>).

Keywords: steel-reinforced concrete beam; high-strength steel reinforcement; flexural performance; shear–span ratio; calculation method

1. Introduction

With the acceleration of urbanization and industrialization, the construction industry has become a major industry in terms of carbon emissions and steel consumption [1–3]. The amount of steel bars used in construction accounts for about 50% of the total steel consumption in the world [4]. The use of high-strength steel bars is an important way to reduce the amount of steel and improve the efficiency of steel use. Low-strength steel bars have been used for a long time. In some high-rise large-span structures, the use of low-strength steel will result in the problem of ‘fat beams and columns’, not only increasing the consumption of steel, but also making them difficult to tie, and more difficult to ensure the quality of concrete pouring. Vigorously promoting high-strength bars in construction projects is an important measure for energy saving and emission reduction and providing engineering structure quality [5,6], which is of great significance for promoting the structural adjustment, transformation, and upgrading of the iron and steel industry and construction. However, existing high-strength bars have poor ductility and toughness and are prone to brittle fracture, which limits their application in engineering structures. CRE bars overcome the contradiction between the high yield strength and high uniform elongation of ordinary high-strength bars. Currently, CRE

materials are mainly used in mining rock engineering. Due to the lack of corresponding analysis and design theories, CRE bars are less often used in concrete structures. Therefore, it has become an important direction for the development of the engineering field to propose a CRE-reinforced concrete structure with excellent mechanical properties and to form a relevant design theory to guide the practice.

High-strength bars refer to the ones with a yield strength of 400 MPa and above. The current Chinese Code for the Design of Concrete Structures (GB 50010-2010) [7] mainly promotes 400 MPa and 500 MPa high-strength bars as longitudinal reinforcement, and 400 MPa bars account for 82.6% of the total amount [8]. The maximum strength grade of steel reinforcement used in Eurocode EN 1992-2: 2004 [9] and American specification ACI 318R-19 [10] is 600 MPa, and the utilization rate of 400–600 MPa high-strength bars is more than 95% [11]. However, there are few applications or studies of reinforcing bars above 700 MPa in concrete structures, especially in civil construction projects.

Constant resistance energy (CRE) bars are a new type of reinforcement formed by a cold-drawing and cold-twisting process on the basis of the new high-strength and high-ductility CRE material with negative Poisson's ratio effect [12] developed by He et al. [13]. The yield strength can reach more than 700 MPa, and the ultimate elongation rate can be more than 20%, surpassing the existing high-strength steel bars with a low elongation rate. CRE material has been applied in many fields for some time, such as deep soft rock mine tunnel support [14,15], highway tunnel support [16], and landslide geologic disaster monitoring and early warning [17], and has achieved more significant economic and social benefits. However, in the field of building engineering, high-strength and high-ductility CRE steel bars are less frequently used in concrete structures. Wang et al. [18,19] and Jiang et al. [20] took the lead in building an intelligent CRE material production line in Qingdao and produced CRE coils and bars. Shao et al. [21] proposed the bond stress–slip constitutive model for CRE reinforcement and marine concrete and found that the mechanical properties of CRE reinforcement, such as yield strength, tensile strength, elongation after break, and total elongation at maximum stress, were significantly higher than those of ordinary reinforcement, and it proved that CRE reinforcement has better bonding properties in concrete. Zhang et al. [2,3] conducted an eccentric compressive test study on concrete columns with CRE reinforcement of 735 MPa yield strength grade as well as a hysteretic performance test study on concrete frame joints, which are the first reports on the testing of CRE-reinforced concrete structures. The study demonstrated that CRE reinforcement has great potential for application in concrete structures in terms of economic, social, and environmental aspects.

At present, the common problem of high-strength reinforcing bars in concrete structures is the low ultimate elongation [22], which leads to the poor ductility and deformation capacity of concrete members with high-strength reinforcing bars, limiting the further application of high-strength reinforcing bars in concrete structures. The CRE bar has the mechanical properties of high strength and high ductility, which can be used in concrete structures to improve the stress performance of the structure. However, there are fewer research results related to the bearing mechanism and calculation method of CRE-reinforced concrete structures, which seriously hinders the promotion and application of CRE reinforcement. In this paper, six CRE-reinforced concrete beams were tested in bending and two HRB-reinforced concrete beams were tested in control tests to investigate the effects of the shear–span ratio and reinforcement type on the mechanical response of the tested beams and to propose a theoretical calculation method for CRE prestressed concrete beams, which will provide a reference and a basis for the application of CRE reinforcement in other types of concrete structures.

2. Test Program

2.1. Test Design

A total of 8 beams were designed for the test, of which 6 were simply supported concrete beams with CRE reinforcement and 2 were simply supported with hot-rolled

ribbed bar 400 (HRB400) reinforcement. The length of the beams was 3500 mm, the concrete strength grade was C35, and the thickness of the protective layer was 15 mm. C35 means that the compressive strength of cubic concrete is 35 MPa. The relevant design parameters of different specimens are shown in Table 1 and the reinforcement is shown in Figure 1.

Table 1. Design parameters for different specimens.

Specimen	Width × Height (mm ²)	Shear–Span Ratio λ	Hoop	Longitudinal Bars in Compression Zone	Longitudinal Bars in Tensile Zone
A-A1	150 × 360	4.57	CRE $\Phi 8@100$	CRE 2 $\Phi 8$	CRE 2 $\Phi 18$
A-A2	150 × 380	4.31	CRE $\Phi 8@100$	CRE 2 $\Phi 8$	CRE 2 $\Phi 18$
A-A3	150 × 420	3.87	CRE $\Phi 8@100$	CRE 2 $\Phi 8$	CRE 2 $\Phi 18$
A-A3'	150 × 420	3.87	HRB400 $\Phi 8@100$	HRB400 2 $\Phi 8$	HRB400 2 $\Phi 18$
A-A4	200 × 400	4.07	CRE $\Phi 8@100$	CRE 2 $\Phi 8$	CRE 3 $\Phi 18$
A-A5	200 × 430	3.77	CRE $\Phi 8@100$	CRE 2 $\Phi 8$	CRE 3 $\Phi 18$
A-A6	200 × 450	3.59	CRE $\Phi 8@100$	CRE 2 $\Phi 8$	CRE 3 $\Phi 18$
A-A6'	200 × 450	3.59	HRB400 $\Phi 8@100$	HRB400 2 $\Phi 8$	HRB400 3 $\Phi 18$

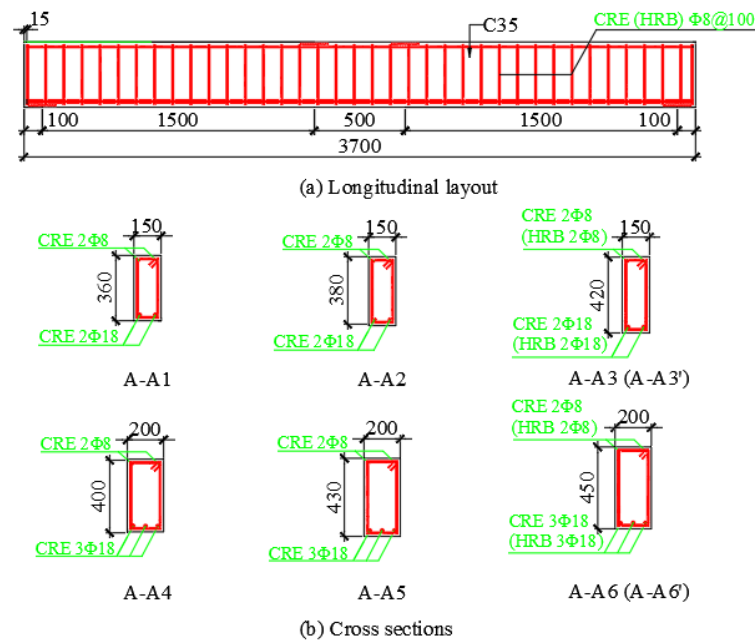


Figure 1. Reinforcements and dimensions of tested beams (unit: mm).

2.2. Test Material

The concrete for this test was made according to the same mix and the strength grade of concrete was C35. The material properties of different types of reinforcement are given in Table 2.

Table 2. Properties of steel bars of different types.

Material	Diameter (mm)	Yield Strength f_y (MPa)	Yield Strain ϵ_y (%)	Ultimate Tensile Strength $f_{s,u}$ (MPa)	Ultimate Tensile Strain $\epsilon_{s,u}$ (%)	Elastic Modulus E_s (GPa)
CRE750	8	750.2	0.568	853.6	20.34	200.90
	18	759.8	0.580	929.7	23.10	201.45
HRB400	8	522.67	0.502	701.3	18.35	200.10
	18	478.67	0.478	689.5	20.55	200.15

2.3. Test Setup and Loading Program

2.3.1. Test Setup

As shown in Figure 2, all beams were subjected to a two-point static load test to simulate distributed loads, with loading points 500 mm apart in the span. Simple support

was achieved using 80 mm diameter solid steel columns (one fixed and the other sliding). Loading was accomplished using 1000 kN hydraulic jacks and recorded by YLR-3 type load cells.

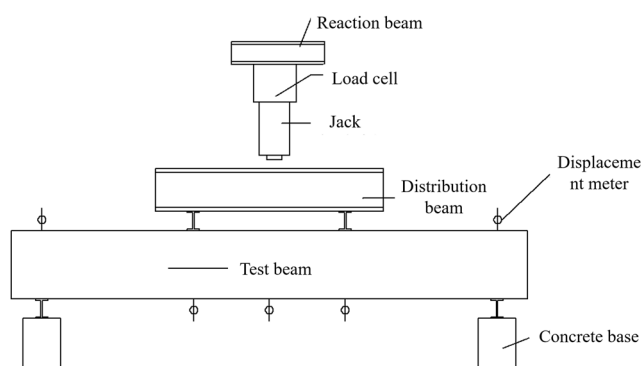


Figure 2. Test setup.

2.3.2. Loading Regime

Monotonic graded loading was used and performed in accordance with the relevant provisions in the Standard for the Test Method of Concrete Structures (GB/T 50152-2012) [23]. Whenever loading to the corresponding load, the load must be held for 10 min; when loading to the normal use of the load, the load must be held for 30 min. The data need to be collected at the load stabilization stage and at the end of the load holding. In the process of loading or load holding, the following phenomena occur, indicating that the tested beam has reached the limit state of bearing capacity: (1) the longitudinal tensile reinforcement in beam bottom pull-off; (2) beam deflection up to the span of $1/50$, which was 70 mm for this test; and (3) compressed concrete crushing.

2.4. Measurement Contents

Three concrete strain gauges were attached to one side of the beam at the mid-span location. One was located on the top surface of the concrete beam and the rest were evenly spaced along the beam height to measure the concrete strain distribution along the section height. Strain gauges were pre-applied to the tensile and compressive longitudinal bars at the mid-span location to measure the strain in the reinforcing bars in the tested beams. The parameters of the strain gauges were as follows: $R = 120 \Omega \pm 0.1 \Omega$, $B \times L = 3 \text{ mm} \times 5 \text{ mm}$, sensitivity factor $2.08 \pm 1\%$. The strain was collected using a DH3818Y static strain tester. The deflection measurement points were arranged along the beam axis at the loading point, mid-span, and at the support. Deflections were measured by displacement meters at the locations shown in Figure 2.

2.5. Specimen Fabrication

All specimen fabrication was performed at the construction site. After the steel bars were discharged, they were firstly tied to ensure the accuracy of the number, type, and position as well as the connecting and anchoring construction measures stipulated in the specifications. Then, the resistance of the strain gauges pasted on the bars was tested to ensure that their resistance value was about 120Ω . The joints of the reinforcing strain gauges were waterproofed to avoid water infiltration into the internal conductors during pouring, leading to strain gauge failure. Finally, the concrete was poured, the specimen was demolded after reaching a certain strength, and artificial watering was carried out for maintenance. In this process, a combination of manual vibration and a vibrating rod was used for vibration to make the concrete dense and uniform.

3. Test phenomenon and Analysis

3.1. Test Phenomenon

The bending test of CRE-reinforced concrete beams is similar to the test process of ordinary reinforced concrete beams, which can be roughly divided into three stages: the uncracked stage, the working stage with cracks, and the failure stage.

3.1.1. Specimens A-A1~A-A6

Specimens A-A1~A-A6 were configured with CRE reinforcement; of these, specimens A-A1~A-A3 were configured with $2\Phi 18$ CRE reinforcement, with a cross-section width of 150 mm and heights of 360 mm, 380 mm, and 420 mm, respectively. Specimens A-A4~A-A6 were configured with $3\Phi 18$ CRE reinforcement, with a cross-section width of 200 mm and heights of 400 mm, 430 mm, and 450 mm, respectively.

The deformation, crack development, and failure characteristics of each test beam during the loading process were basically the same. At the early stage of loading, the specimens showed elastic characteristics, the sections were not cracked, the deflections increased approximately linearly, and the reinforcement stresses and concrete strains were small. When the load was further increased to about $0.15 P_{u,c} \sim 0.2 P_{u,c}$ ($P_{u,c}$ is the calculated value of ultimate load capacity), one or more vertical cracks appeared in the test beam near the cross-section of the pure bending section in the span middle. With the further application of load, new cracks were continuously generated, and the original cracks continuously extended from the beam bottom to the loading edge, and the width of the cracks became larger.

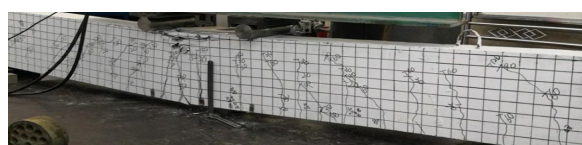
When the load was increased to a certain level, the crack development of the specimen was relatively stable, with no new main cracks produced and the crack spacing stabilized. When the load was increased to 123 kN, 132 kN, 148 kN, 208 kN, 223 kN, and 235 kN, the longitudinal tensile reinforcement of specimens A1~A6 reached yielding in each case, and the specimens began to enter the plastic state. With continuing increases in the load, the deflection and crack width of the specimens increased faster, and secondary cracks appeared locally with a small width. As shown in Figure 3, close to the destruction, the main crack width of the specimen increased rapidly, the concrete in the compression zone was crushed quickly, and the specimen underwent appropriate reinforcement failure. The ultimate bearing capacities of specimens A1~A6 were 145.51 kN, 155.58 kN, 175.45 kN, 240.46 kN, 264.04 kN, and 279.46 kN, respectively.



(a) Specimen A-A1



(b) Specimen A-A2



(c) Specimen A-A3



(d) Specimen A-A4



(e) Specimen A-A5

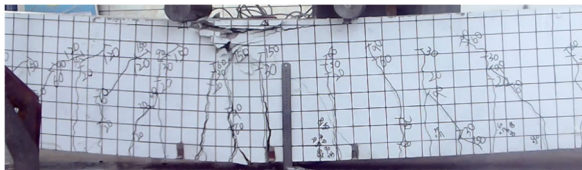


(f) Specimen A-A6

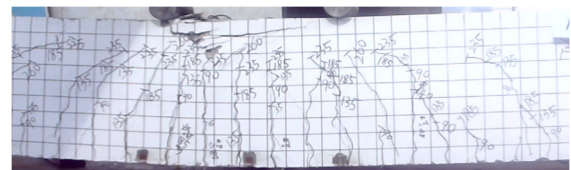
Figure 3. Crack distribution of CRE-reinforced concrete beams.

3.1.2. Specimens A-A3' and A-A6'

Specimens A-A3' and A-A6' were concrete beams with HRB400 reinforcement. Among them, specimen A-A3' was configured with 2 Φ 18 HRB400 bars, and the cross-section size was the same as that of A-A3. Specimen A-A6' was configured with 3 Φ 18 HRB400 bars, and the cross-section size was the same as that of A-A6. These two beams also experienced reinforcement failure, which was the same as that of the beams with CRE reinforcement. The longitudinal tensile reinforcement in specimens A-A3' and A-A6' yielded loads of 117 kN and 193 kN, respectively. The failure of ordinary reinforced concrete beams is shown in Figure 4 with ultimate loads of 122.69 kN and 195.58 kN, respectively.



(a) Specimen A-A3'



(b) Specimen A-A6'

Figure 4. Crack distribution of HRB-reinforced concrete beams.

3.2. Analysis of Test Results

3.2.1. Bending Moment–Deflection Curve

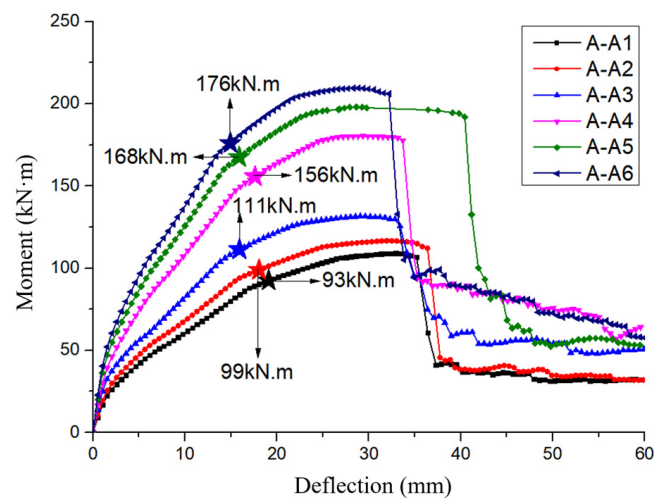
(1) Specimens A-A1~A-A6

Specimens A-A1~A-A6 were configured with CRE reinforcement, and the comparison of bending moment–deflection curves is shown in Figure 5. It can be seen that the shape of the moment–deflection curves is basically the same. At the beginning of loading, the deflections of each test beam increased approximately linearly, and the larger the beam cross-section, the greater the bending stiffness. With the increase in loading and the cracking of concrete, the stiffness of the specimens decreased, and the curves show some nonlinearity. As shown in Table 3, the cracking moments of specimens A-A1~A-A6 were 12 kN·m, 16 kN·m, 20 kN·m, 24 kN·m, 22 kN·m, and 35 kN·m. At the same width, the flexural stiffness of the section decreases with the increase in the shear–span ratio, and thus the cracking load decreases. Compared to specimen A-A1, the cracking load of specimen A-A3 increased by 67%. Compared to specimen A-A1, the cracking load of specimen A-A3 is increased by 46%.

The yield moments of specimens A-A1~A-A6 were 93 kN·m, 99 kN·m, 111 kN·m, 156 kN·m, 168 kN·m, and 176 kN·m, respectively, as shown in Figure 5 and Table 3, with the corresponding deflections at yielding in the range of 15 mm~20 mm. After the yielding of the longitudinal tensile reinforcement, the test beams started to enter the plastic phase, the stiffness became smaller, and the deflection growth accelerated, while the bearing capacity continued to increase. After reaching the ultimate load, the deflection of the test beams increased rapidly, and all of them declined after maintaining a certain flexural bearing capacity. The concrete in the compression zone was crushed, and appropriate reinforcement failure occurred. The ultimate bearing capacities of specimens A-A1~A-A6 were 109.13 kN·m, 116.69 kN·m, 131.59 kN·m, 180.35 kN·m, 198.03 kN·m, and 209.60 kN·m. Compared with specimen A-A1, the ultimate bearing capacities of specimens A-A2 and A-A3 increased by 6.92% and 20.58%, respectively. Compared to specimen A-A4, the ultimate bearing capacity of specimens A-A5 and A-A6 increased by 9.81% and 16.22%, respectively. As the height of the beam section increases, the cracking resistance and ultimate load-carrying capacity of the test beams also increase.

Table 3. Structural response of different specimens.

Specimen	Measured Cracking Moment $M_{cr,r}$ (kN·m)	Measured Cracking Deflection $y_{cr,r}$ (mm)	Measured Yield Moment $M_{y,r}$ (kN·m)	Measured Yield Deflection $y_{y,r}$ (mm)	Measured Ultimate Moment $M_{u,r}$ (kN·m)	Measured Ultimate Deflection $y_{u,r}$ (mm)
A-A1	12.00	0.70	93.00	19.57	109.13	22.40
A-A2	16.00	0.84	99.00	19.40	116.69	24.80
A-A3	20.00	0.61	111.00	16.00	131.59	22.20
A-A3'	19.00	0.74	88.00	11.00	92.02	12.95
A-A4	24.00	0.76	156.00	17.51	180.35	24.38
A-A5	22.00	0.62	168.00	16.60	198.03	20.00
A-A6	35.00	0.79	176.00	15.00	209.60	20.00
A-A6'	33.00	0.77	145.00	11.00	146.69	12.00

**Figure 5.** Bending moment–deflection curves (with CRE bars).

(2) Specimens A-A3, A-A3', A-A6, and A-A6'

Specimens A-A3 and A-A3' were configured with 2 Φ 18 CRE bars and 2 Φ 18 HRB400 bars, respectively, with a cross-section of 150 mm \times 420 mm. Specimens A-A6 and A-A6' were configured with 3 Φ 18 CRE bars and 3 Φ 18 HRB400 bars, respectively, with a cross-section of 200 mm \times 450 mm. The comparison of the moment–deflection curves of the two beams is shown in Figure 6. It can be seen that the initial bending stiffness of the beams with CRE reinforcement is basically the same as that of the beams with HRB400 reinforcement when the beam cross-section size and reinforcement area are the same. As shown in Table 3, the cracking moments of specimens A-A3 and A-A3' were 20 kN·m and 19 kN·m, respectively, and the cracking moment of A-A3 was about 5% higher than that of A-A3'. The cracking moments of specimens A-A6 and A-A6' were 35 kN·m and 33 kN·m, respectively. The cracking load of A-A6 was about 4% higher than that of A-A6'. The cracking resistance of CRE-reinforced concrete beams was slightly higher than that of HRB-reinforced concrete beams.

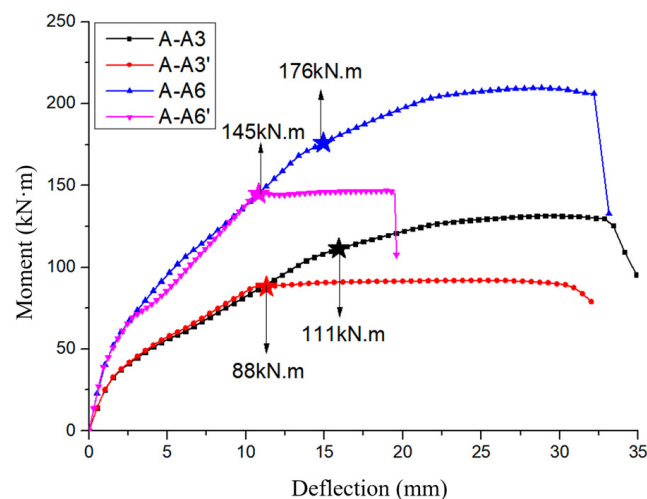
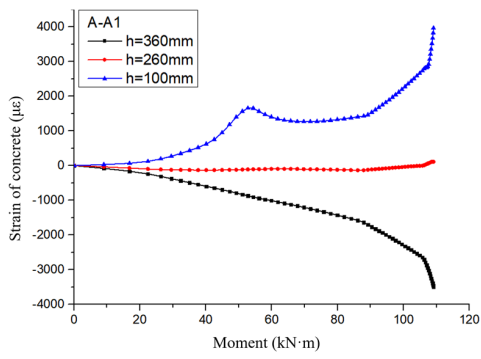


Figure 6. Bending moment–deflection curves (Comparison between CRE and HRB bars).

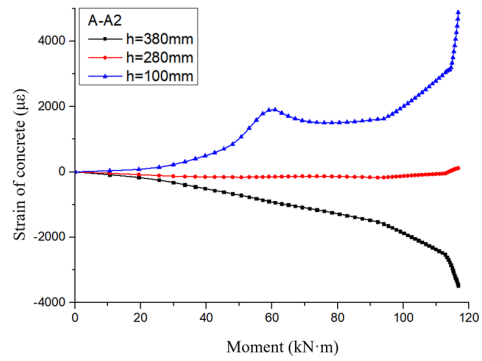
Before the yielding of the reinforcement, both beams showed good elastic properties. After yielding, the deflection of the beams configured with HRB400 reinforcement increased rapidly and the load-carrying capacity remained basically unchanged, showing good plastic deformation ability. Meanwhile, the beams configured with CRE reinforcement continued to increase the load-carrying capacity after the yielding of the reinforcement, but the stiffness decreased, and the deflection increased faster than before the yielding of the reinforcement. At yielding, the bending moments corresponding to specimens A-A3 and A-A3' were 111 kN·m and 88 kN·m, respectively. The yield load of A-A3 was about 26% higher than that of A-A3', and the corresponding deflections were 16 mm and 11 mm, respectively. The bending moments corresponding to specimens A-A6 and A-A6' were 176 kN·m and 145 kN·m, respectively. It can be seen that the concrete beams configured with CRE reinforcement corresponded to a greater deflection at yield. When the beams failed, the ultimate bending moments corresponding to specimens A-A3 and A-A3' were 131.59 kN·m and 92.02 kN·m, respectively, and the former was about 43% higher than the latter. The corresponding ultimate moments of specimens A-A6 and A-A6' were 209.60 kN·m and 146.69 kN·m, respectively, and the former was about 42.89% higher than the latter. After reaching the ultimate moment, both beams lost their load-bearing capacity and failed.

3.2.2. Strain Curve of Concrete

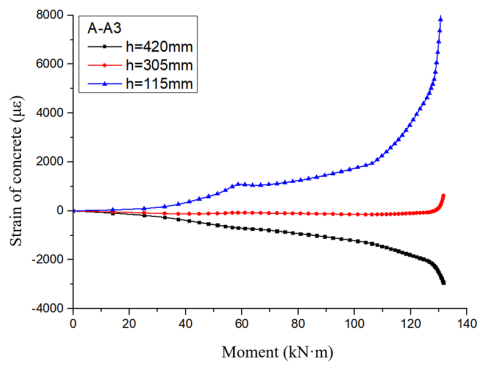
Concrete strain–moment curves and concrete strain distributions along the section height for specimens A-A1 to A-A6 are given in Figures 7 and 8, respectively. h is the distance of the strain gauges from the bottom surface of the beam. Concrete strains at the tensile side edges were replaced by tensile reinforcement strains. With the increase in load, the change rule of the concrete strain of each specimen is basically the same. At the beginning of loading, with the increase in load, the concrete strain increased nearly linearly. The cracking through the location resulted in the concrete tensile strain curve inflection point. The strain grows faster, and then the concrete tensile strain tends to grow steadily again after the crack development has stabilized. When the ultimate load was reached, the maximum compressive strains of concrete in specimens A-A1~A-A6 were 3498 $\mu\epsilon$, 3490 $\mu\epsilon$, 2951 $\mu\epsilon$, 3560 $\mu\epsilon$, 3481 $\mu\epsilon$, and 3280 $\mu\epsilon$, respectively, which were close to or exceeded the ultimate compressive strain of concrete of 3300 $\mu\epsilon$, indicating that the concrete was crushed in the end.



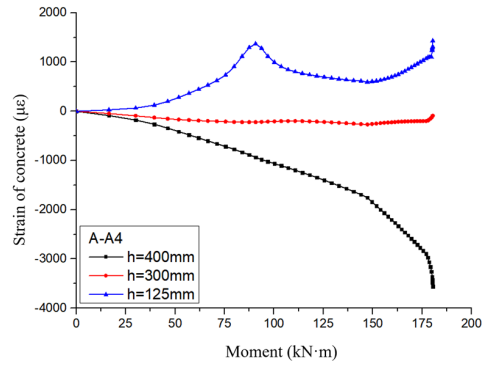
(a) Specimen A-A1



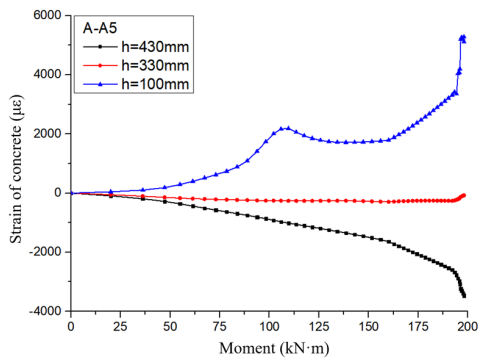
(b) Specimen A-A2



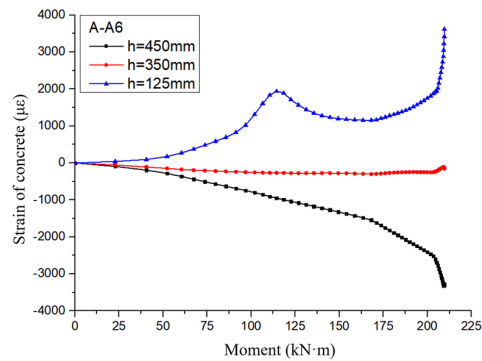
(c) Specimen A-A3



(d) Specimen A-A4

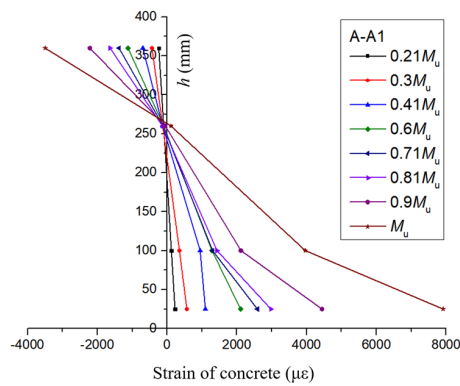


(e) Specimen A-A5

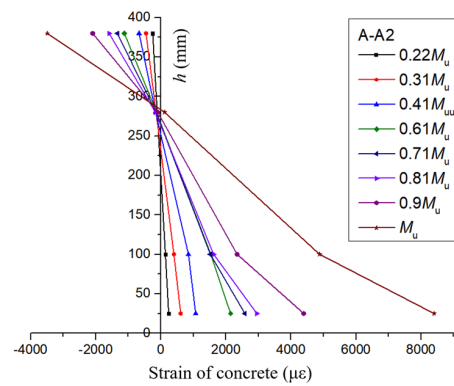


(f) Specimen A-A6

Figure 7. Concrete strain-moment curves.



(a) Specimen A-A1



(b) Specimen A-A2

Figure 8. Cont.

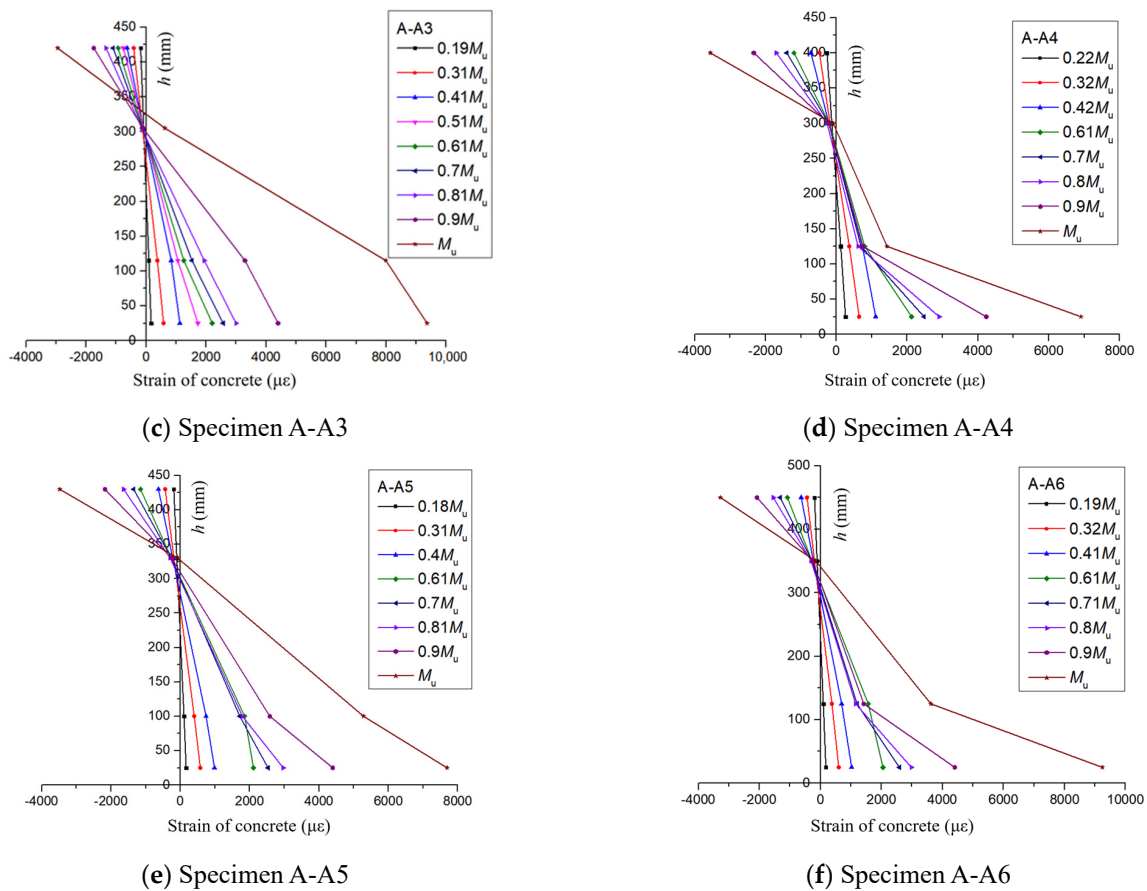


Figure 8. Concrete strain distribution along section heights.

From the concrete strain distribution along the beam height given in Figure 8, it can be seen that the mid-span cross-section strain of each test beam configured with CRE reinforcement basically conforms to the flat cross-section assumption. In particular, for test specimens A-A1~A-A3, the height of the concrete compression zone is about 95 mm, and for test specimens A-A4~A-A6, the height is about 100 mm.

3.2.3. Strain Curve of Steel Bars

A comparison of strain–moment curves of the longitudinal bars for specimens A-A1~A-A6 is shown in Figure 9, where measurement points 1 and 1' indicate the tensile and compressive longitudinal bars in the middle of the span, respectively. With the increase in load, the change rule of the longitudinal bar strain of each specimen is basically the same. At the beginning of loading, the reinforcement strain increased linearly with the increase in load, and the smaller the beam height, the faster the reinforcement strain grew. When reaching the mid-span ultimate bending moment, the longitudinal tensile reinforcement strains of specimens A-A1~A-A6 were 7916 $\mu\epsilon$, 8401 $\mu\epsilon$, 9364 $\mu\epsilon$, 6906 $\mu\epsilon$, 7694 $\mu\epsilon$, and 9236 $\mu\epsilon$, respectively, which all exceeded the yield strain of 5800 $\mu\epsilon$ for the CRE reinforcement. Meanwhile, the longitudinal compressive reinforcement strains were $-2758 \mu\epsilon$, $-2762 \mu\epsilon$, $-2478 \mu\epsilon$, $-2918 \mu\epsilon$, $-2861 \mu\epsilon$, and $-2778 \mu\epsilon$, respectively, and no yielding occurred.

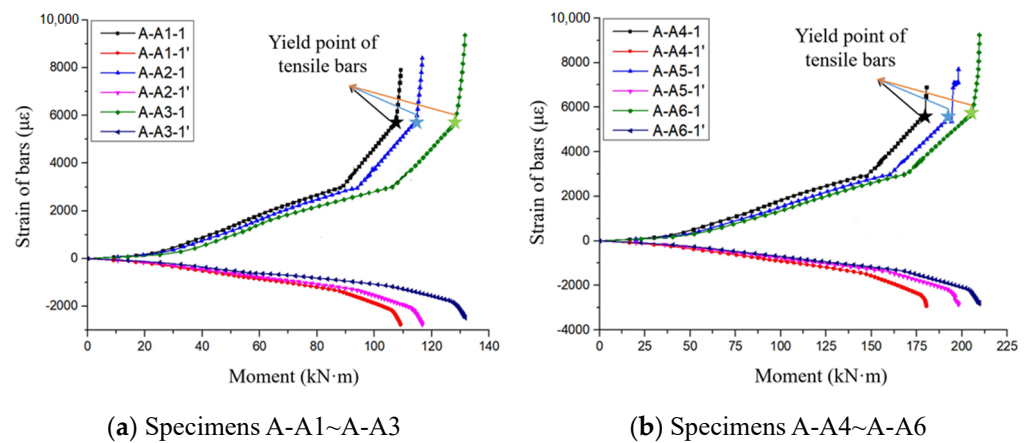


Figure 9. Strain-moment curves of longitudinal bars in CRE-reinforced concrete beams.

The strain–moment curves of the longitudinal bars of specimens A-A3 vs. A-A3' and A-A6 vs. A-A6' are given in Figure 10. It can be seen that the longitudinal tensile reinforcement of the beams configured with CRE and HRB400 reinforcements yielded. When the beam cross-section size and reinforcement area were the same, the longitudinal bar strain increased at about the same rate in both beams before the longitudinal tensile reinforcement yields. After yielding, the longitudinal tensile reinforcement strains of both beams grew rapidly. At the time of failure, the strains in the compressive reinforcement of both the beams configured with CRE and HRB400 reinforcements were low, about $2000 \mu\epsilon$, which had not yet reached the strain corresponding to the yield strength.

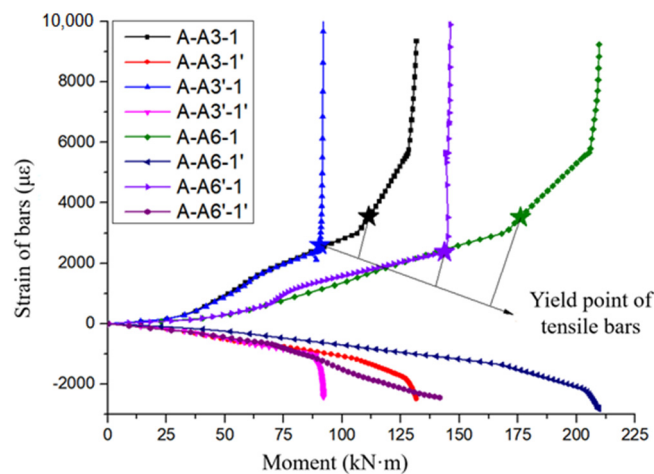


Figure 10. Strain-moment curves for different types of longitudinal bars.

4. Theoretical Analysis

4.1. Basic Assumptions and Constitutive Relation Model

The basic assumptions mainly include: (1) the concrete strain along the height direction conforms to the flat section assumption, i.e., the cross-section concrete strain is linearly distributed along the height direction; (2) there exists a good bond between the longitudinal stress reinforcement and the concrete, and there is no slippage between the two; and (3) a bifurcated model is used to model the stress–strain relationship of longitudinal tension reinforcement. As shown in Figure 11, the length of the beam is l , the width is b , and the height is h_1 ; the elastic modulus of the top longitudinal reinforcement, the area, and the distance from the concrete top are E_{s1} , A_{s1} , and d_{s1} , respectively; the elastic modulus of the longitudinal reinforcement bottom, the area, and the distance from the concrete top are E_{s2} , A_{s2} , and d_{s2} , respectively. The elastic modulus and sectional area of the concrete are E_c and A_c , respectively. The height of the neutral axis is d_c .

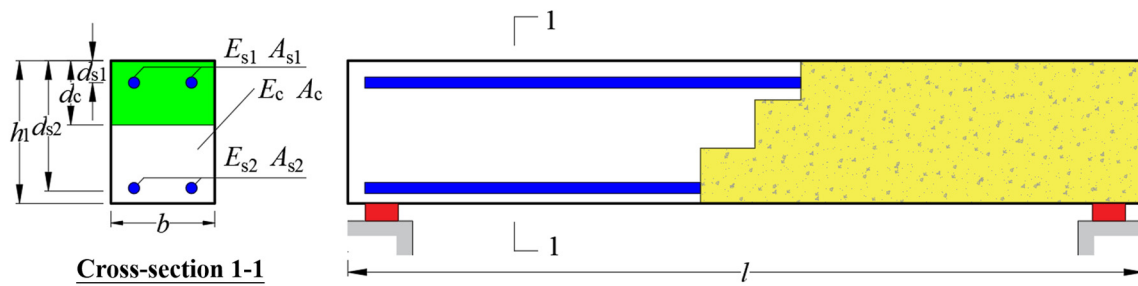


Figure 11. Cross-sectional drawing and beam length.

The stress–strain relationship of the concrete in the compression zone is based on the concrete constitutive model given in the current Code for the Design of Concrete Structures (GB 50010-2010) [7], as shown in Figure 12 below. The stress–strain relationship of concrete under pressure is:

$$\sigma_c = \begin{cases} f'_c \left[\alpha_a \left(\frac{\varepsilon}{\varepsilon_c} \right) + (3 - 2\alpha_a) \left(\frac{\varepsilon}{\varepsilon_c} \right)^2 + (\alpha_a - 2) \left(\frac{\varepsilon}{\varepsilon_c} \right)^3 \right] & \varepsilon < \varepsilon_c \\ f'_c \left[\frac{2\varepsilon_u - \varepsilon_c}{2(\varepsilon_u - \varepsilon_c)} - \frac{\varepsilon}{2(\varepsilon_u - \varepsilon_c)} \right] & \varepsilon_c < \varepsilon < \varepsilon_u \end{cases} \quad (1)$$

where, α_a is the parameter corresponding to the ascending section of the stress–strain relationship curve in uniaxial compression, and its value is $2.4 - 0.0125f'_c$; α_d is the parameter corresponding to the descending section of the stress–strain relationship curve in uniaxial compression, and its value is $-0.905 + 0.157(f'_c)^{0.785}$; f'_c is the compressive strength of concrete; ε_c is the peak compressive strain corresponding to a concrete stress of f'_c , and its value is $(700 + 172\sqrt{f'_c}) \times 10^{-6}$; ε_u is the concrete stress equal to $0.5f'_c$ in the descending section of the concrete stress–strain relationship curve corresponding to the strain of concrete, and its value is $\varepsilon_c [1 + 2\alpha_a + \sqrt{(1 + 4\alpha_d)}] / (2\alpha_d)$.

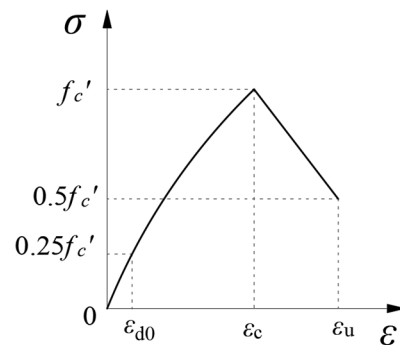


Figure 12. Stress–strain relationship for concrete under compression.

The elastic modulus E_c of concrete is obtained according to the American code ACI 318R-19 [10]:

$$E_c = 4700\sqrt{f'_c} \quad (2)$$

From Figure 12, it can be seen that when the concrete stress is less than $0.25f'_c$, the stress and strain of concrete show an approximately linear relationship. When the concrete stress is $0.25f'_c$, the corresponding strain of concrete is ε_{d0} . The relationship between stress and strain applied to concrete in tension is:

$$\sigma_c(\varepsilon) = E_c\varepsilon \quad (3)$$

When the concrete tensile strain reaches the ultimate tensile strain ε_{ct} , the concrete is subjected to the ultimate tensile stress f_t and cracking of the concrete occurs. The ultimate tensile stress f_t of concrete can be obtained from the American code ACI 318R-19 [10]:

$$f_t = 0.62\sqrt{f'_c} \quad (4)$$

The stress–strain relationship for longitudinal reinforcement is:

$$\sigma_s = \begin{cases} E_s \varepsilon & |\varepsilon| < \varepsilon_y \\ f_y + k_y(\varepsilon - \varepsilon_y) & \varepsilon_y < |\varepsilon| < \varepsilon_{s,u} \end{cases} \quad (5)$$

where E_s is the elastic modulus of the reinforcement; f_y is the yield strength of the reinforcement; $f_{s,u}$ is the ultimate tensile strength of the reinforcement; ε_y and $\varepsilon_{s,u}$ are the strain corresponding to the yield strength and the ultimate tensile strength of the reinforcement; k_y is the stress enhancement coefficient of the ordinary reinforcement, the value of which is $(f_{s,u} - f_y)/(\varepsilon_{s,u} - \varepsilon_y)$.

4.2. Analysis of Forces and Deformations in the Linear Elastic Phase

The stress and strain in the concrete of the beams under loading satisfy the flat section assumption, as shown schematically in Figure 13.

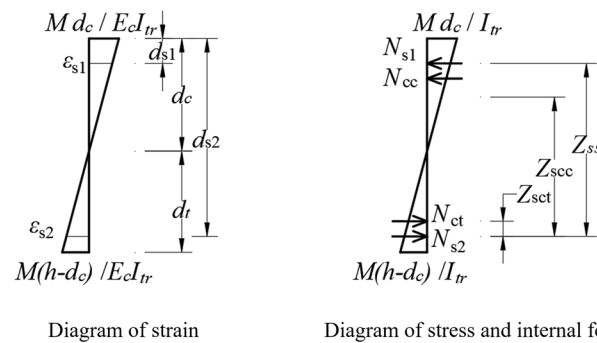


Figure 13. Concrete stress change under prestressing action.

In Figure 13, I_{tr} is the converted cross-sectional moment of inertia. d_t is the height of the concrete in the tension zone. ε_{s1} and ε_{s2} are the strains in the concrete at the positions of the compression longitudinal bar and the tension longitudinal bar, respectively. N_{cc} , N_{ct} , N_{s1} , and N_{s2} are the axial forces on the concrete in the compression zone, the concrete in the tension zone, the compression longitudinal bar, and the tension longitudinal bar, respectively. Z_{sct} , Z_{scc} , and Z_{ss} are the distances between the prestressing bars, the concrete in the compression zone, and the top longitudinal bar to the bottom longitudinal bar, respectively. M is the external bending moment.

$$A_{tr} = bh_1 + \left(\frac{E_{s1}}{E_c} - 1\right)A_{s1} + \left(\frac{E_{s2}}{E_c} - 1\right)A_{s2} \quad (6)$$

$$d_c = \frac{A_c \frac{h_1}{2} + \left(\frac{E_{s1}}{E_c} - 1\right)A_{s1}d_{s1} + \left(\frac{E_{s2}}{E_c} - 1\right)A_{s2}d_{s2}}{A_{tr}} \quad (7)$$

$$I_{tr} = \frac{bh_1^3}{12} + bh_1 \left(d_c - \frac{h_1}{2}\right)^2 + \left(\frac{E_{s1}}{E_c} - 1\right)A_{s1}(d_{s1} - d_c)^2 + \left(\frac{E_{s2}}{E_c} - 1\right)A_{s2}(d_{s2} - d_c)^2 \quad (8)$$

where A_{tr} is the converted cross-sectional area. As shown in Figure 13, the stress f_{cb} at the bottom of the concrete can be expressed as:

$$f_{cb} = \frac{M(h_1 - d_c)}{I_{tr}} \quad (9)$$

With the increase in external load, the concrete at the beam bottom is gradually tensioned until it reaches the ultimate tensile stress f_t . At this time, cracking failure occurs in the concrete beam. By substituting Equations (6)–(8) into Equation (9), the cracking moment can be calculated according to Equation (10):

$$M_{cr} = \frac{f_t I_{tr}}{h_1 - d_c} \quad (10)$$

The deflection of the concrete beam under cracking moment can be obtained by Equation (11):

$$y_{cr} = k \frac{M_{cr} l^2}{E_c I_{tr}} \quad (11)$$

where: $k = 1/12$ (single concentrated load), $23/216$ (two-point concentrated load), and $5/48$ (uniform load).

4.3. Analysis of Forces and Deformations during the Working Phase with Cracks

When the concrete beam cracks, the neutralization axis rises rapidly along the height direction, and the structure undergoes roughly the following three phases: (1) the compressive stress of the concrete changes linearly; (2) the compressive stress of the concrete changes partially nonlinearly, and the tensile reinforcement reaches yielding; and (3) the tensile reinforcement yields and the compressive stress of the concrete changes partially nonlinearly.

In Figure 14, ε_{cc} is the compressive strain of the top concrete; ε_{ct} is the peak strain of the concrete in tension; d_z is the height of the concrete in the compression zone; h_{cr} is the height of the crack. When the concrete beam is in stage 1, the top compressive strain of concrete ε_{cc} is less than ε_{d0} , and the compressive stress and strain of the concrete are considered to be linearly related. According to the flat section assumption of strain and the deformation coordination condition, the strain distribution of each part of the concrete beam is shown in Figure 14. According to the constitutive relationship of each material, the stress and internal force diagrams of each part can be obtained. The relationship between ultimate tensile strain and compressive strain of concrete is established as shown in Figure 14:

$$\frac{\varepsilon_{ct}}{\varepsilon_{cc}} = \frac{d_t}{d_c} = a_1 \quad (12)$$

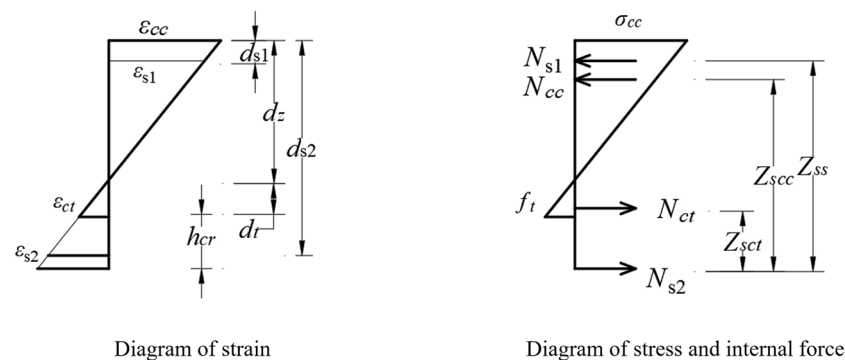


Figure 14. Strain, stress, and internal force distribution of stage 1.

It is assumed that there is a complete bond between the concrete and the ordinary reinforcement, i.e., the reinforcement strain is the same as the concrete strain at the same

location. In addition, the concrete strain along the height direction satisfies the flat section assumption. Therefore, the relationship between the strain of ordinary reinforcement and the strain of concrete is shown below:

$$\varepsilon_{s2} = \frac{\varepsilon_{cc}(d_{s2} - d_z)}{d_z} \quad (13)$$

$$\varepsilon_{s1} = \frac{\varepsilon_{cc}(d_z - d_{s1})}{d_z} \quad (14)$$

The axial force balance and bending moment balance are established as shown in Figure 14:

$$N_{s1} + N_{cc} - N_{ct} - N_{s2} = 0 \quad (15)$$

$$M = N_{s1}Z_{ss} + N_{cc}Z_{scc} - N_{ct}Z_{sct} \quad (16)$$

The constitutive relations and positions of the parts are substituted into Equations (15) and (16):

$$A_{s1}E_{s1}\varepsilon_{s1} + \int_{h_1-d_z}^{h_1} b\sigma_{cc}(y)dy - \left[\int_{h_1-d_z-d_t}^{h_1-d_z} b\sigma_{ct}(y)dy + A_{s2}E_{s2}\varepsilon_{s2} \right] = 0 \quad (17)$$

$$M = A_{s1}E_{s1}\varepsilon_{s1}(d_{s2} - d_{s1}) + \int_{h_1-d_z}^{h_1} b\sigma_{cc}(y)dy \left(d_{s2} - \frac{d_z}{3} \right) - \int_{h_1-d_z-d_t}^{h_1-d_z} b\sigma_{ct}(y)dy \left(d_{s2} - d_z - \frac{2d_t}{3} \right) \quad (18)$$

Since the compressive strain and compressive stress of concrete are linearly related, the axial force equation is further simplified by substituting Equations (12)–(14) into (17):

$$A_{s1}E_{s1} \frac{\varepsilon_{cc}(d_z - d_{s1})}{d_z} + \frac{1}{2}bd_z\varepsilon_{cc}E_c - \frac{1}{2}ba_1d_zf_t - A_{s2}E_{s2} \frac{\varepsilon_{cc}(d_{s2} - d_z)}{d_z} = 0 \quad (19)$$

Further, Equation (19) is transformed to obtain the neutralization axis height d_z :

$$d_z = \frac{\sqrt{(A_{s1}E_{s1}\varepsilon_{cc} + A_{s2}E_{s2}\varepsilon_{cc})^2 + 2b(E_c\varepsilon_{cc} - a_1f_t)(A_{s1}E_{s1}\varepsilon_{cc}d_{s1} + A_{s2}E_{s2}\varepsilon_{cc}d_{s2})} - (A_{s1}E_{s1}\varepsilon_{cc} + A_{s2}E_{s2}\varepsilon_{cc})}{b(E_c\varepsilon_{cc} - a_1f_t)} \quad (20)$$

Once the compressive strain ε_{cc} at the concrete top is determined, the neutral axis height d_z can be calculated by Equation (20), which leads to the height of the tensile zone d_t , the strains in each part, and the axial force of the tensile reinforcement N_{s2} . Substituting each of the calculated parameters in Equation (18), the corresponding external bending moments M can be obtained. Unlike other existing analytical methods, this method can determine the crack height h_{cr} :

$$h_{cr} = h_1 - (d_z + d_t) \quad (21)$$

When the height of the concrete neutralization axis d_z and the height of the tension zone d_t are determined, the area of the cracked section is:

$$A_{cr} = b(d_z + d_t) + \left(\frac{E_{s1}}{E_c} - 1 \right) A_{s1} + \left(\frac{E_{s2}}{E_c} - 1 \right) A_{s2} \quad (22)$$

The distance from the mass center of the cracked section to the top concrete is:

$$d_{cr} = \frac{(d_z + d_t)^2 \frac{b}{2} + \left(\frac{E_{s1}}{E_c} - 1 \right) A_{s1}d_{s1} + \left(\frac{E_{s2}}{E_c} - 1 \right) A_{s2}d_{s2}}{A_{cr}} \quad (23)$$

The moment of inertia I_{cr} for the cracked section is:

$$I_{cr} = \frac{b(d_z + d_t)^3}{12} + b(d_z + d_t) \left[d_{cr} - \frac{(d_z + d_t)}{2} \right]^2 + \left(\frac{E_{s1}}{E_c} - 1 \right) A_{s1} (d_{s1} - d_{cr})^2 + \left(\frac{E_{s2}}{E_c} - 1 \right) A_{s2} (d_{s2} - d_{cr})^2 \quad (24)$$

According to the current Code for the Design of Concrete Structures (GB 50010-2010) [7], the stiffness B_s can be calculated:

$$B_s = \frac{0.85 E_c I_{tr}}{\frac{M_{cr}}{M} + \left(1 - \frac{M_{cr}}{M} \right) \left[\left(1 + \frac{0.21}{n_{s2} \rho} \right) - 0.7 \right]} \quad (25)$$

where n_{s2} is the ratio of the elastic modulus of the tension reinforcement to the elastic modulus of the concrete, i.e., E_{s2}/E_c ; ρ is the reinforcement ratio of longitudinal tension reinforcement, i.e., A_{s2}/bd_{s2} . Under the action of the external bending moment, the deflection of the concrete beam is:

$$y = k \frac{Ml^2}{B_s} \quad (26)$$

When the concrete beam is in stage 2, the top compressive strain ϵ_{cc} of the concrete is between ϵ_{d0} and ϵ_c , and the compressive stress of the concrete is considered to have a partially nonlinear relationship with the compressive strain until the plain bonded reinforcement or prestressing reinforcement reaches yielding. According to the flat section assumption of strain, the deformation coordination condition, and the intrinsic relationship of each material, the distribution of strain, stress, and internal force in each part of the concrete beam is shown in Figure 15. In Figure 15, d_1 is the height of linear variation in concrete stress and compressive strain; N_{cc1} and N_{cc2} are the axial forces due to linear and nonlinear variations in concrete stress and compressive strain, respectively; Z_{scc1} and Z_{scc2} are the distances from N_{cc1} and N_{cc2} to tensile reinforcement, respectively; σ_{d0} is the stress corresponding to a concrete strain of ϵ_{d0} ; and σ_{a1} is the average stress of the nonlinear part. The relationship between ultimate tensile strain, ϵ_{d0} , and compressive strain of concrete is established as shown in Figure 15:

$$\frac{\epsilon_{ct}}{\epsilon_{cc}} = \frac{d_t}{d_z} = a_1 \quad (27)$$

$$\frac{\epsilon_{d0}}{\epsilon_{cc}} = \frac{d_1}{d_z} = a_2 \quad (28)$$

Through the constitutive relationship of concrete, the average compressive stress σ_{a1} of concrete can be expressed as:

$$\sigma_{a1}(\epsilon) = \sum_{i=0}^n \frac{1}{2(n+1)} \left[\sigma_c \left(\frac{(i+1)\epsilon}{n+1} \right) + \sigma_c \left(\frac{i\epsilon}{n+1} \right) \right] , \quad \epsilon_{d0} \leq \epsilon \leq \epsilon_c \quad (29)$$

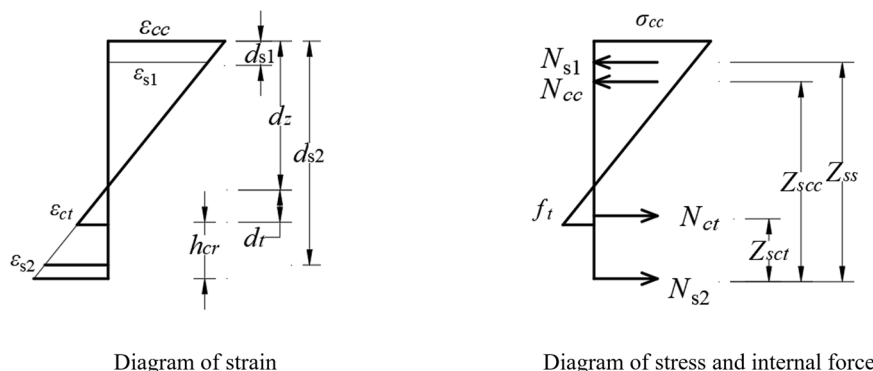


Figure 15. Strain, stress, and internal force distribution for stages 2 and 3.

The axial force balance and bending moment balance are established as shown in Figure 15:

$$N_{s1} + N_{cc1} + N_{cc2} - N_{ct} - N_{s2} = 0 \quad (30)$$

$$M = N_{s1}Z_{ss} + N_{cc2}Z_{scc2} + N_{cc1}Z_{scc1} - N_{ct}Z_{sct} \quad (31)$$

The constitutive relations and positions of the parts are substituted into Equations (30) and (31):

$$A_{s1}E_{s1}\varepsilon_{s1} + \int_{h_1-d_z}^{h_1} b\sigma_{cc}(y)dy - \left[\int_{h_1-d_z-d_t}^{h_1-d_z} b\sigma_{ct}(y)dy + A_{s2}E_{s2}\varepsilon_{s2} \right] = 0 \quad (32)$$

$$M = A_{s1}E_{s1}\varepsilon_{s1}(d_{s2} - d_{s1}) + \int_{h_1-(d_z-d_1)}^{h_1} b\sigma_{cc}(y)dy \left(d_{s2} - \frac{(d_z-d_1)}{2} \right) + \int_{h_1-d_z}^{h_1-(d_z-d_1)} b\sigma_{cc}(y)dy \left(d_{s2} - (d_z - d_1) - \frac{d_1}{3} \right) - \int_{h_1-d_z-d_t}^{h_1-d_z} b\sigma_{ct}(y)dy \left(d_{s2} - d_z - \frac{2d_t}{3} \right) \quad (33)$$

Equation sets (1)–(5), (27), and (28) are substituted into Equations (32) and (33), and the axial force equation and bending moment equation can be further simplified as:

$$A_{s1}E_{s1}\varepsilon_{s1} + \sigma_{a1}b(d_z - d_1) + \frac{1}{2}\sigma_{d0}bd_1 - \left(\frac{1}{2}f_tbd_t + A_{s2}E_{s2}\varepsilon_{s2} \right) = 0 \quad (34)$$

$$M = A_{s1}E_{s1}\varepsilon_{s1}(d_{s2} - d_{s1}) + \sigma_{a1}b(d_z - d_1) \left(d_{s2} - \frac{(d_z-d_1)}{2} \right) + \frac{1}{2}\sigma_{d0}bd_1 \left(d_{s2} - (d_z - d_1) - \frac{d_1}{3} \right) - \frac{1}{2}f_tbd_t \left(d_{s2} - d_z - \frac{2d_t}{3} \right) \quad (35)$$

Further, Equation (35) is transformed to obtain the neutralization axis height d_z :

$$d_z = \frac{\sqrt{(A_{s1}E_{s1}\varepsilon_{cc} + A_{s2}E_{s2}\varepsilon_{cc})^2 + 2[2\sigma_{a1}b(1-a_2) + b\sigma_{d0} - b\sigma_{a1}f_t](A_{s1}E_{s1}\varepsilon_{cc}d_{s1} + A_{s2}E_{s2}\varepsilon_{cc}d_{s2}) - (A_{s1}E_{s1}\varepsilon_{cc} + A_{s2}E_{s2}\varepsilon_{cc})}}{2\sigma_{a1}b(1-a_2) + b\sigma_{d0} - b\sigma_{a1}f_t} \quad (36)$$

Similar to Stage 1, once the strain ε_{cc} of the concrete top has been determined, the neutralization axis height d_z for stage 2 can be calculated using Equations (30) and (36), which in turn leads to the height of the tensile zone, d_t , the strains in the various sections, and the axial force of the tensile reinforcement, N_{s2} . Substituting the calculated parameters into Equations (35) and (21), the corresponding external bending moments M and crack heights h_{cr} are obtained. The deflections y under the corresponding external bending moments are obtained by using the set of Equations (22) to (26). The top compressive strains ε_{cc} of the concrete in stage 3, after the tensile reinforcement reaches yielding, are between ε_{d0} and ε_c . According to the flat section assumption of strain, the strain of concrete along the height direction satisfies a linear relationship. According to the strain coordination condition, the strain of the reinforcement at the same location is the same as that of the concrete. From Equation (5), the stress after yielding of the reinforcement is further expressed as:

$$f_s = f_y + k_y \left[\frac{\varepsilon_{cc}}{d_z} (d_{s2} - d_z) - \varepsilon_y \right] \quad (37)$$

The relationship between the stress and axial force of the reinforcement can be expressed as:

$$N_{s2} = f_{s2}A_{s2} \quad (38)$$

Substituting Equations (37) and (38) into Equation (34), the axial force equation can be expressed as:

$$A_{s2} \left\{ f_y + k_y \left[\frac{\varepsilon_{cc}}{d_z} (d_{s2} - d_z) - \varepsilon_y \right] \right\} + A_{s1}E_{s1}\varepsilon_{s1} + \sigma_{a1}b(d_z - d_1) + \frac{1}{2}\sigma_{d0}bd_1 - \frac{1}{2}f_tbd_t = 0 \quad (39)$$

Further, Equation (39) is transformed to obtain the neutralization axis height d_z :

$$d_z = \frac{\sqrt{[A_{s1}E_{s1}\epsilon_{cc} - f_y A_{s2} + A_{s2}k_y(\epsilon_{cc} + \epsilon_y)]^2 + 2[2\sigma_{a1}b(1 - a_2) + ba_2\sigma_{d0} - ba_1f_{ct}](A_{s1}E_{s1}\epsilon_{cc}d_{s1} + k_yA_{s2}\epsilon_{cc}d_{s2}) - [A_{s1}E_{s1}\epsilon_{cc} - f_y A_{s2} + A_{s2}k_y(\epsilon_{cc} + \epsilon_y)]}{2\sigma_{a1}b(1 - a_2) + ba_2\sigma_{d0} - ba_1f_{ct}} \quad (40)$$

Once the strain ϵ_{cc} of the concrete at the top is determined, the neutral axis height d_z can be calculated by Equation (40), which in turn leads to the height of the tensile zone d_t , and the strains in each part. Substituting the calculated parameters into Equation (35), the corresponding external bending moment M is obtained. y , the deflection under the corresponding external bending moment, is obtained using Equation (26).

4.4. Analysis of Forces and Deformations in the Extreme Failure Stage

As shown in Figure 16, the compressive stress of concrete partially varies nonlinearly. After all the longitudinal bars yield, the strain in the top concrete is greater than the strain corresponding to the peak stress until the ultimate compressive strain ϵ_u is reached.

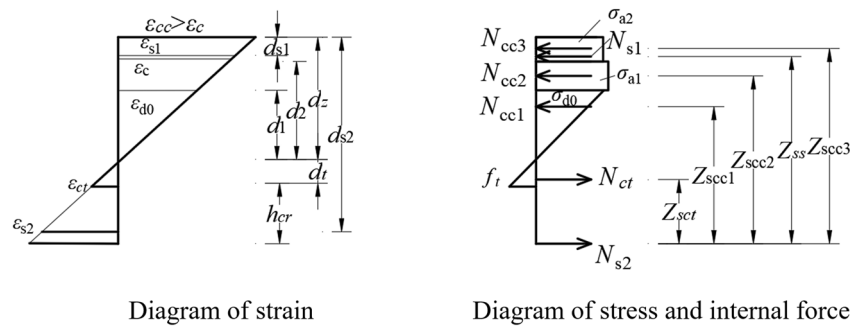


Figure 16. Strain, stress, and internal force distribution in the ultimate stage.

As shown in Figure 16, d_2 is the distance from the position where the strain is ϵ_c to the neutral axis; N_{cc3} is the axial force corresponding to the descending section of compressive stress; Z_{scc3} is the distance from N_{cc3} to the tensile reinforcement; and σ_{a2} is the average stress in the descending section of compressive stress. Relationships between the ultimate concrete tensile strain, ϵ_{d0} , ϵ_c , the strain of the compressive reinforcement, and the compressive strain of the top concrete are established:

$$\frac{\epsilon_{ct}}{\epsilon_{cc}} = \frac{d_t}{d_z} = a_1 \quad (41)$$

$$\frac{\epsilon_{d0}}{\epsilon_{cc}} = \frac{d_1}{d_z} = a_2 \quad (42)$$

$$\frac{\epsilon_c}{\epsilon_{cc}} = \frac{d_2}{d_z} = a_3 \quad (43)$$

$$\frac{\epsilon_{cc}}{d_z}(d_z - d_{s1}) = \epsilon_{s1} \quad (44)$$

Through the constitutive relationship of concrete, the average compressive stress σ_{a2} of concrete can be approximated as:

$$\sigma_{a2} = \frac{f'_c + \sigma_c(\epsilon)}{2} \quad (45)$$

The axial force equilibrium and bending moment equilibrium are expressed as follows, respectively:

$$N_{s1} + N_{cc1} + N_{cc2} + N_{cc3} - N_{ct} - N_{s2} = 0 \quad (46)$$

$$M = N_{s1}Z_{ss} + N_{cc3}Z_{scc3} + N_{cc2}Z_{scc2} + N_{cc1}Z_{scc1} - N_{ct}Z_{sct} \quad (47)$$

Substituting the material's constitutive relationship into Equations (46) and (47):

$$A_{s1}E_{s1}\varepsilon_{s1} + \sigma_{a2}b(d_z - d_2) + \sigma_{a1}b(d_2 - d_1) + \frac{1}{2}\sigma_{d0}bd_1 - \left(\frac{1}{2}f_tbd_t + f_{s1}A_{s2}\right) = 0 \quad (48)$$

$$M = A_{s1}E_{s1}\varepsilon_{s1}(d_{s2} - d_{s1}) + \sigma_{a1}b(d_2 - d_1)\left(d_{s2} - (d_z - d_2) - \frac{(d_2 - d_1)}{2}\right) + \frac{1}{2}\sigma_{d0}bd_1\left(d_{s2} - (d_z - d_1) - \frac{d_1}{3}\right) + \sigma_{a2}b(d_z - d_2)\left(d_{s2} - \frac{(d_z - d_2)}{2}\right) - \frac{1}{2}f_tbd_t\left(d_{s2} - d_z - \frac{2d_t}{3}\right) \quad (49)$$

Further, Equation (49) is transformed to obtain the neutralization axis height d_z :

$$d_z = \frac{\sqrt{[A_{s1}E_{s1}\varepsilon_{cc} - f_yA_{s2} + A_{s2}k_y(\varepsilon_{cc} + \varepsilon_y)]^2 + 2[2\sigma_{a2}b(1 - a_3) + 2\sigma_{a1}b(a_3 - a_2) + ba_2\sigma_{d0} - ba_1f_t](A_{s1}E_{s1}\varepsilon_{cc}d_{s1} + k_yA_{s2}\varepsilon_{cc}d_{s2})} - [A_{s1}E_{s1}\varepsilon_{cc} - f_yA_{s2} + A_{s2}k_y(\varepsilon_{cc} + \varepsilon_y)]}{2\sigma_{a2}b(1 - a_3) + 2\sigma_{a1}b(a_3 - a_2) + ba_2\sigma_{d0} - ba_1f_t} \quad (50)$$

Once the strain ε_{cc} of the top concrete is determined, the neutral axis height d_z can be calculated by Equation (50), which in turn leads to the height of the tensile zone d_t , the strains in each part, and the axial force of the tensile reinforcement N_{s2} . Substituting each of the calculated parameters in Equation (49), the corresponding external bending moments M are obtained. The deflections y under the corresponding external bending moments are obtained by using the set of Equations (22) to (26).

4.5. Theoretical Model Validation

In this paper, six CRE-reinforced concrete beams and two HRB-reinforced concrete beams were subjected to bending tests, and the forces and deformations of each member at the critical stage were compared to verify the reliability of the theoretical model in this paper. The comparison of the theoretical and measured values of the loads at the critical stage is shown in Table 4; the average value of the ratio between the two at different stages is 1.02 at the maximum and the coefficient of variation is 0.133. The comparison of the theoretical and measured values of the deflection at the key stage is shown in Table 5; the average value of the two ratios at different stages is 1.18 and the coefficient of variation is 0.135. The measured and theoretical values are in good agreement, which indicates that the theoretical model has high accuracy and reliability.

Table 4. Theoretical and measured values of loads at the critical stage.

Specimen	Measured Cracking Moment $M_{cr,r}$ (kN·m)	Theoretical Cracking Moment $M_{cr,e}$ (kN·m)	$M_{cr,e}/M_{cr,r}$	Measured Yield Moment $M_{y,r}$ (kN·m)	Theoretical Yield Moment $M_{y,e}$ (kN·m)	$M_{y,e}/M_{y,r}$	Measured Ultimate Moment $M_{u,r}$ (kN·m)	Theoretical Ultimate Moment $M_{u,e}$ (kN·m)	$M_{u,e}/M_{u,r}$
A-A1	12.00	14.52	1.21	93.00	94.50	1.02	109.13	100.66	0.92
A-A2	16.00	16.05	1.00	99.00	100.39	1.01	116.69	120.16	1.03
A-A3	20.00	19.32	0.97	111.00	111.14	1.00	131.59	135.77	1.03
A-A3'	19.00	23.89	1.00	88.00	155.73	1.00	92.02	187.76	1.04
A-A4	24.00	27.31	1.24	156.00	170.48	1.01	180.35	205.32	1.04
A-A5	22.00	29.71	0.85	168.00	178.19	1.01	198.03	217.00	1.04
A-A6	35.00	19.30	1.02	176.00	91.62	1.04	209.60	92.21	1.00
A-A6'	33.00	29.67	0.90	145.00	148.49	1.02	146.69	148.65	1.01
Average value			1.02			1.02			1.01
Variation coefficient			0.133			0.012			0.040

Table 5. Theoretical and measured values of deflections at the critical stage.

Specimen	Measured Cracking Deflection $y_{cr,r}$ (mm)	Theoretical Cracking Deflection $y_{cr,e}$ (mm)	$y_{cr,e}/y_{cr,r}$	Measured Yield Deflection $y_{y,r}$ (mm)	Theoretical Yield Deflection $y_{y,e}$ (mm)	$y_{y,e}/y_{y,r}$	Measured Ultimate Deflection $y_{u,r}$ (mm)	Theoretical Ultimate Deflection $y_{u,e}$ (mm)	$y_{u,e}/y_{u,r}$
A-A1	0.97	0.70	1.39	17.96	19.57	0.92	19.15	22.40	0.86
A-A2	0.92	0.84	1.10	16.83	19.40	0.87	20.21	24.80	0.81
A-A3	0.83	0.61	1.36	14.79	16.00	0.92	18.15	22.20	0.82
A-A3'	0.88	0.76	1.15	15.96	17.51	0.91	19.30	24.38	0.79
A-A4	0.82	0.62	1.33	14.79	16.60	0.89	17.87	20.00	0.89
A-A5	0.78	0.79	0.98	13.92	15.00	0.93	17.02	20.00	0.85
A-A6	0.83	0.74	1.12	12.16	11.00	1.11	12.40	12.95	0.96
A-A6'	0.78	0.77	1.01	11.59	11.00	1.05	11.67	12.00	0.97
Average value			1.18			0.95			0.87
Variation coefficient			0.135			0.09			0.077

4.6. Application and Discussion

In the experiment, the influence of shear span-to-depth ratio and the type of reinforcing steel on the flexural performance of concrete beams reinforced with corrosion-resistant steel (CRE) was examined. The theoretical framework presented in this paper has been validated for the reliability of CRE-reinforced concrete beams. A parametric analysis of the theory was conducted to investigate the impact of concrete strength, tensile steel area, and compressive steel area on the flexural performance of CRE-reinforced concrete beams, thereby further exploring the load-carrying mechanisms of such components.

In the design phase, concrete strength primarily affects the cracking moment of the structure. Increasing the area of tensile steel is aimed at enhancing the ultimate load-carrying capacity of the structure. Similarly, increasing the area of compressive steel is intended to improve the stress state of the top concrete and, consequently, enhance the ultimate load-carrying capacity of the structure. In this specific example, certain parameters remain consistent with the previous experiments. The beam length is 3500 mm, the beam width is 150 mm, and the beam height is 360 mm. The diameter of the stirrups is 8 mm, and the spacing between stirrups is 100 mm. Both longitudinal steel reinforcements in the tensile and compressive zones are made of CRE steel. The concrete strength, and the quantity and diameter of the longitudinal steel reinforcements in the tensile and compressive zones for each component are shown in Figure 1. Taking the component labeled as “C35-T2-C4” as an example, “C35” indicates that the concrete strength of the component is C35, “T2” signifies that there are two CRE steel reinforcements with a diameter of 18 mm in the tensile zone, and “C4” denotes four CRE steel reinforcements with a diameter of 8 mm in the compressive zone.

Under the influence of various factors, the load–displacement curves of the specimens are depicted in Figure 17. The enhancement of concrete strength, as well as the augmentation of the areas of tensile and compressive steel reinforcement, all contribute to an elevation in the structural cracking moment. The former is a consequence of heightened concrete strength, which in turn increases its tensile strength. The latter two are attributable to the amplification of steel reinforcement areas, which augments the structural flexural stiffness, thus influencing the structural cracking moment. In the event of structural failure, the tensile CRE steel reinforcement yields, while the compressive CRE steel reinforcement remains and does not yield. In comparison to concrete strength and the area of compressive CRE steel reinforcement, the augmentation of the tensile CRE steel reinforcement area can substantially increase the structural ultimate load. When the number of tensile CRE steel reinforcements increases from two to six, the structural load-bearing capacity is enhanced by 31.4%. Therefore, for CRE steel-reinforced concrete structures, it is advisable to prioritize the augmentation of the tensile steel reinforcement area and the reinforcement of the uppermost concrete to enhance the structural load-bearing capability.

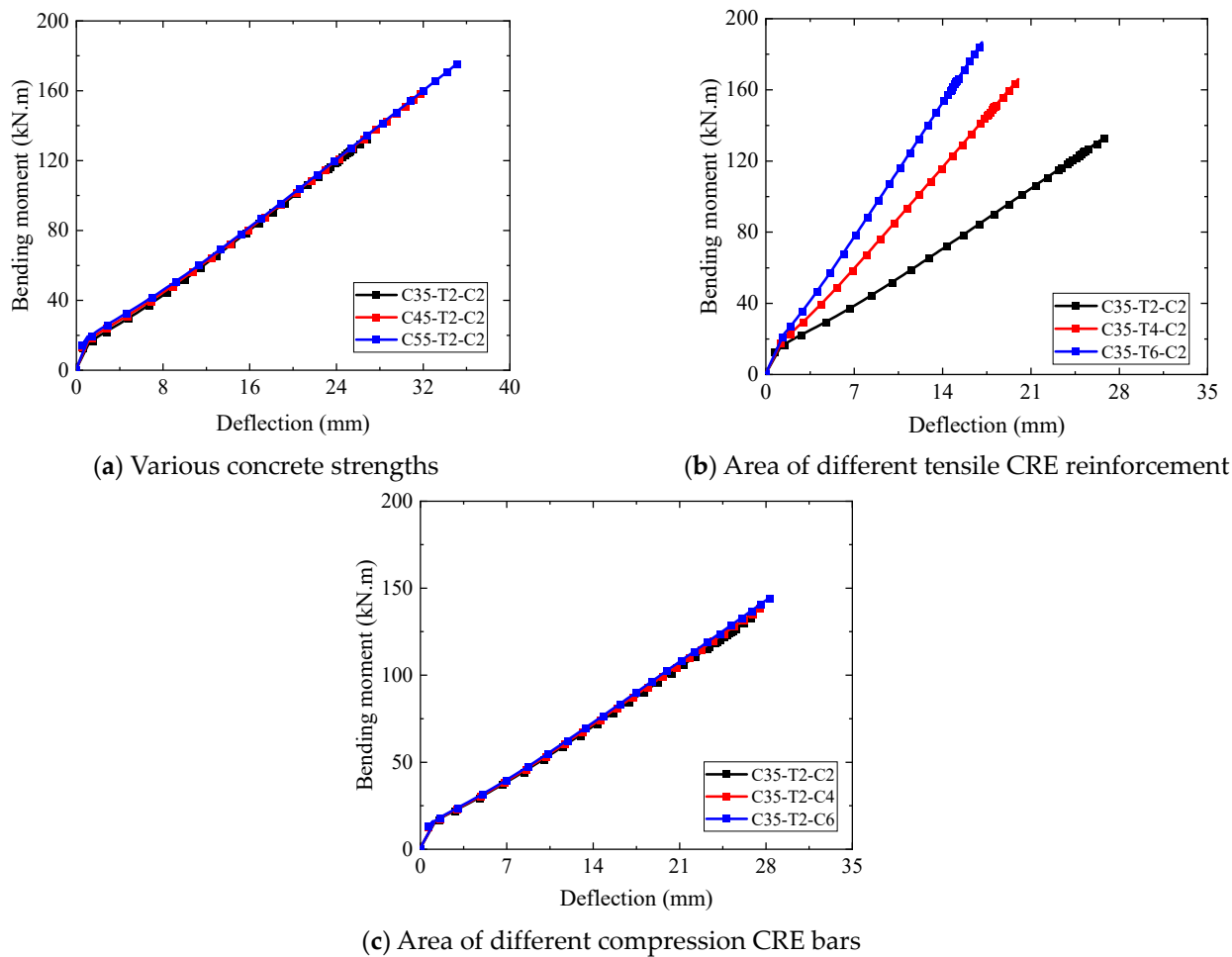


Figure 17. Load–displacement curves for different variables.

5. Conclusions

In this paper, the bearing mechanism and analysis method of CRE-reinforced concrete beams are systematically studied, and the results of bending tests of six CRE-reinforced concrete beams and two HRB-reinforced concrete beams are reported. The effects of different shear–span ratios and reinforcement types on the performance of the structure are analyzed, and the calculation method of the structural response of such members is proposed, which provides a reference and basis for the application of CRE reinforcement in other types of concrete structures. The main conclusions are as follows:

- (1) When appropriate reinforcement failure occurs, the force characteristics of CRE-reinforced concrete beams are the same as those of ordinary reinforced concrete beams, i.e., yielding of tensile reinforcement occurs; the tensile reinforcement yields first at the time of failure, followed by crushing of concrete in the compression zone.
- (2) The cracking resistance and load-carrying capacity of CRE-reinforced concrete beams are improved with decreasing shear–span ratio for the same width. For the same shear–span ratio, the cracking and ultimate loads of the specimen with a section height of 420 mm are 67% and 20.58% higher, respectively, than those of the specimen with a section height of 360 mm.
- (3) Under the same conditions, the load-carrying capacity of CRE-reinforced concrete beams is higher than that of HRB-reinforced concrete beams, with the former having about 43% higher ultimate load than the latter. In addition, the difference in cracking moments between the two is not significant.

- (4) In case of structural failure, CRE reinforcement used as tensile reinforcement can reach its yield strength and utilize its tensile properties, but CRE reinforcement used as compressive reinforcement cannot reach its yield strength.
- (5) Comparison of measured and theoretical values of forces and deformations of each member at the critical stage shows that the calculation method proposed in this paper for the bending performance of CRE-reinforced concrete beams can calculate the mechanical response of such members efficiently and safely, and the results of the calculations have good accuracy. Through theoretical analysis, prioritizing increasing the area of tensile CRE reinforcement and reinforcing the concrete at the top can enhance the load-carrying capacity of the structure.

Inevitably, there are shortcomings in this paper, such as the lack of corresponding finite element parametric analyses; beams are often under-exploited in terms of the mechanical properties of CRE reinforcement due to the destruction of the concrete at the top. Therefore, the concrete in the compression zone can be strengthened and such specimens can be analyzed subsequently.

Author Contributions: Conceptualization, X.Z., L.S. and P.W.; data curation, X.Y. and Y.S.; formal analysis, Y.S., L.S. and P.W.; funding acquisition, P.W.; investigation, Y.S. and P.W.; project administration, P.W.; resources, P.W.; software, X.Y.; supervision, L.S.; validation, X.Z. and Y.S.; writing—original draft, X.Z.; writing—review and editing, X.Z. All authors have read and agreed to the published version of the manuscript.

Funding: This research was funded by National Natural Science Foundation of China, with the grant number of 52127814.

Data Availability Statement: Data is contained within the article.

Acknowledgments: The authors wish to acknowledge support from the National Natural Science Foundation of China (52127814).

Conflicts of Interest: The authors declare no conflict of interest.

References

1. Zhou, Y.; Hu, D.; Wang, T.; Tian, H.; Gan, L. Decoupling effect and spatial-temporal characteristics of carbon emissions from construction industry in China. *J. Clean. Prod.* **2023**, *419*, 138243. [[CrossRef](#)]
2. Zhang, X.; Ding, Y.; Wang, X.; Sun, L. Study on eccentric compressive behavior of concrete columns reinforced with CRE735 high-strength steel bars. *Buildings* **2023**, *13*, 188. [[CrossRef](#)]
3. Zhang, X.; Han, F.; Wang, X.; Sun, L.; Wang, Q.; Wang, P. Research on seismic performance of 735 MPa high-strength reinforced concrete frame joints. *Buildings* **2023**, *13*, 320. [[CrossRef](#)]
4. En, L.K.; Rahiman, N.A.; Othman, N.; Ali, K.N.; Wah, L.Y.; Moayed, F.; Dzahir, M.A.M. Quantification process of carbon emissions in the construction industry. *Energy Build.* **2023**, *289*, 113025.
5. Zhao, J.; Jiang, Y.; Li, X. Flexural behavior of concrete beams reinforced with high-strength steel bars after exposure to elevated temperatures. *Constr. Build. Mater.* **2023**, *382*, 131317. [[CrossRef](#)]
6. Fu, T.; Zhu, Z.; Li, Y.; Xu, L.; Sun, Y.; Sun, Y.; Meng, L.; Sun, Z. Restoring force model of hollow prefabricated square pier with grouted sleeves connection and high-strength steel bars. *Soil Dyn. Earthq. Eng.* **2023**, *169*, 107868. [[CrossRef](#)]
7. GB 50010-2010; Code for Design of Concrete Structures. Standards Press of China: Beijing, China, 2010. (In Chinese)
8. Li, Y.; Li, S.; Qiao, J.; Pan, J. Experimental research on bond behaviour between high-strength steel bars and ultra-high-performance fibre-reinforced concrete. *Structures* **2023**, *50*, 859–869. [[CrossRef](#)]
9. EN 1992-2:2004; Eurocode 2: Design of Concrete Structures. British Standard: London, UK, 2004.
10. American Concrete Institute (ACI). *Building Code Requirements for Structural Concrete (ACI 318-19) and Commentary (ACI 318R-19)*; American Concrete Institute: Farmington Hills, MI, USA, 2019.
11. Zhang, Y.; Xiong, X.; Liang, Y.; He, M. Study on flexural behavior of concrete beams reinforced with hybrid high-strength and high-toughness (HSHT) and ordinary steel bars. *Eng. Struct.* **2023**, *285*, 115978.
12. Gao, Y. Auxetic metamaterials and structures. *J. Mater. Eng.* **2021**, *49*, 38–47. (In Chinese)
13. He, M.C.; Li, C.; Gong, W.L.; Wang, J.; Tao, Z. Support principles of CRE bolts/cables and control techniques of large deformation. *Chin. J. Rock Mech. Eng.* **2016**, *35*, 1513–1529.
14. He, M.; Du, S.; Gong, W.; Nie, W. Mechanical characteristics and engineering applications of bolt/cable with negative poisson's ratio. *Mech. Eng.* **2022**, *44*, 75–87.

15. He, M.; Guo, Z. Mechanical property and engineering application of anchor bolt with constant resistance and large deformation. *Chin. J. Rock Mech. Eng.* **2014**, *33*, 1297–1308.
16. Wang, Q.; Xu, S.; Xin, Z.; He, M.; Wei, H.; Jiang, B. Mechanical properties and field application of constant resistance energy-absorbing anchor cable. *Tunn. Undergr. Space Technol.* **2022**, *125*, 104526.
17. Wang, Q.; Xu, S.; He, M.; Jiang, B.; Wei, H.; Wang, Y. Dynamic mechanical characteristics and application of constant resistance energy-absorbing supporting material. *Int. J. Min. Sci. Technol.* **2022**, *32*, 447–458.
18. Wang, Q.; He, M.C.; Xu, S.; Xin, Z.X.; Jiang, B.; Wei, H.Y. Mechanical properties and engineering application of constant resistance energy absorbing bolt. *J. China Coal Soc.* **2022**, *47*, 3397–3407.
19. Wang, Q.; Wu, W.; Wang, Y.; He, M.; Xue, H.; Wei, H. Evolution and control mechanism of rockburst in rock anchored by new energy-absorbing material. *Rock Mech. Rock Eng.* **2023**, *56*, 4569–4582. [[CrossRef](#)]
20. Jiang, B.; Xin, Z.; Zhang, X.; Deng, Y.; Wang, M.; Li, S.; Ren, W. Mechanical properties and influence mechanism of confined concrete arches in high-stress tunnels. *Int. J. Min. Sci. Technol.* **2023**, *33*, 829–841. [[CrossRef](#)]
21. Shao, S.W.; Shang, H.S.; Feng, H.B.; Wang, W.Z. Study on the mechanical properties of NPR steel bars and the bonding properties with marine concrete. *Constr. Build. Mater.* **2022**, *316*, 125721. [[CrossRef](#)]
22. Yang, X.; Yuan, H.; Li, C.; Wu, L.; Wang, P.; Liu, Y.; Jiang, B.; Wang, Q.; Zhang, X.; Liu, F.; et al. Experimental studies on behavior of failed CRB750 steel bars reinforced concrete beams retrofitted with steel plate. *Eng. Struct.* **2021**, *243*, 112539. [[CrossRef](#)]
23. *GB/T 50152-2012*; Standard for Test Method of Concrete Structures. Standards Press of China: Beijing, China, 2012. (In Chinese)

Disclaimer/Publisher’s Note: The statements, opinions and data contained in all publications are solely those of the individual author(s) and contributor(s) and not of MDPI and/or the editor(s). MDPI and/or the editor(s) disclaim responsibility for any injury to people or property resulting from any ideas, methods, instructions or products referred to in the content.